www.sciencemag.org/cgi/content/full/316/5832/1729/DC1

Supporting Online Material for

Deformation of $(Mg,Fe)SiO_3$ Post-Perovskite and D″ Anisotropy

Sébastien Merkel,* Allen K. McNamara, Atsushi Kubo, Sergio Speziale,
Lowell Miyagi, Yue Meng, Thomas S. Duffy, Hans-Rudolf Wenk

*To whom correspondence should be addressed. E-mail: sebastien.merkel@univ-lille1.fr

Published 22 June 2007, *Science* **316**, 1729 (2007)
DOI: 10.1126/science.1140609

This PDF file includes:

Supporting Online Material

1 Experimental details

High-pressures and high-temperatures were generated in a laser-heated diamond anvil cell with large openings to allow radial x-ray diffraction. The sample was loaded in a 40-μm diameter hole in a beryllium gasket preindented to 30-μm thickness and compressed with beveled diamond anvils. Diffraction patterns were collected in radial geometry (Fig. S1) with a Mar345 image plate detector (3450 pixels diameter) and a monochromatic incident x-ray beam ($\lambda = 0.3684$ Å) on the 16-ID-B beamline of the High Pressure Collaborative Access Team (HPCAT) sector of the Advanced Photon Source (APS). Sample to detector distance and detector non-orthogonality were determined using a CeO_2 standard prior to the experiment. Laser heating was performed by focusing a Nd:YLF laser ($\lambda = 1053$ nm) to a 30-μm spot and temperature was measured by thermal radiance spectrometry. The diffraction patterns were collected with a $\pm 2.5^\circ$ ω-oscillation around the z-axis (Fig. S1) in order to increase the number of grains contributing to the diffraction. To improve the signal to noise ratio and overcome local saturation on the image plate, multiple exposures (up to 20, with 60 to 90 seconds accumulation for each spectrum) were collected and summed before processing.

Starting material, $(Mg_{1.80}Fe_{0.18}Al_{0.01}Ca_{0.01})Si_2O_6$, was the same powder of natural orthopyroxene previously studied in Ref. (*S1*), mixed with 10 wt% platinum. The sample was compressed directly to high pressure. We could not observe coherent diffraction from

within the sample after cold compression. The sample was then heated to about 1700 K for 20 min and 2000 K for 15 min. After temperature quenching, the diffraction peaks of the pPv phase were observed and the pressure estimated to 145 GPa from the equation of state of pPv synthesized from the same starting material (*S1*). After 22 hours, pressure was increased to 150 GPa and later to 157 GPa 7 hours later. At each pressure increment, diffraction was measured in radial geometry. Because of the large uncertainties on the equation of state of post-perovskite and deviatoric stresses in the experiment, we estimate that our uncertainty on pressure is significant (at least 10 GPa). However, for this study, accurate pressure determination is not critical.

2 Data processing

The spectra contain diffraction lines from pPv and Pt in addition to Be and BeO from the gasket. Be and BeO peaks are very intense compared to those of the sample. Diffraction peaks of Pt however were weak and difficult to identify. On the other hand, many peaks of (Mg,Fe)SiO_3-pPv do not overlap with Be or BeO and can be fully analyzed. The two-dimensionnal diffraction images are converted into one-dimensionnal diffraction patterns by binning the data in sections of 10° of the azimuth angle δ. For each 1-D pattern, we identify the 022, 132, 113, 004, 114, and 152+062+200 diffraction lines of pPv phase and fit their positions and intensities using the commercial software Peakfit.

Samples in these experiments are subjected to a non-hydrostatic stress, where the principal stress in the loading direction σ_3 is greater than the radial stress σ_1 imposed by the gasket. The angle χ between the diffracting plane normal and the maximum stress axis (Fig. S1) can be calculated from the azimuth angle on the detector δ with the relation

$$\cos\chi = \cos\theta\cos\delta, \tag{1}$$

where θ is the diffraction angle. Assuming a Reuss-Voigt-Hill micromechanical model and neglecting the effect of plasticity and lattice preferred orientations, the measured d-spacings vary with χ as

$$d_m(hkl) = d_P(hkl)\left[1 + (1 - 3\cos^2\chi)Q(hkl)\right], \tag{2}$$

where $d_m(hkl)$ is the measured d-spacing, $d_P(hkl)$ the d-spacing under the equivalent hydrostatic pressure P, and $Q(hkl)$ is a measure of the strain induced by the differential stress (*S2*).

The fitted $d_P(hkl)$ are used to calculate unit cell paramaters of the pPv phase and the corresponding equivalent hydrostatic pressures. The fitted $Q(hkl)$ are used to estimate the differential stress component supported by the sample with the relation

$$t = \sigma_3 - \sigma_1 \approx 6G < Q(hkl) >, \tag{3}$$

where G is the shear modulus of the aggregate (*S2*).

Variations of the d-spacings of the (022), (132) and (113) planes of pPv with χ are shown in Fig. S2 along with results from least-square fits of equation 2. Table S1 presents the unit cell paramaters a, b, c, average lattice strains $< Q(hkl) >$ and differential stress components t we obtain using the equation of state measured in Ref. (*S1*) and the shear modulus calculated in Ref. (*S3*).

The relative intensity variations of the diffraction peaks are used to calculate the orientation distribution function (ODF) of the sample using the WIMV algorithm, as implemented in the software Beartex (*S4*). The ODF contains all information about the crystallite orientations and can be used for deformation mechanisms analysis. For each orientation g, the ODF $f(g)$ describes the probability density of finding crystallites that have the orientation g within dg. We have

$$f(g) > 0; \quad \frac{1}{8\pi^2}\int_G f(g)dg = 1. \tag{4}$$

The degree of orientation in the sample is expressed by the texture index F_2 defined as

$$F_2 = \frac{1}{8\pi^2} \int_G [f(g)]^2 \, dg. \tag{5}$$

For a material with random texture, the texture index F_2 is equal to 1, for a textured material $F_2 > 1$.

Texture indices obtained in the experiment are presented in Table S1 and Fig. S3 presents the measured diffraction intensities for the 122, 132, 113, 004, 114, and 152+062+200 diffraction lines of pPv at 145 GPa along with those recalculated from the ODF.

3 Convection numerical model

The two-dimensional convection calculation employed a Rayleigh number of 10^7, stress-free boundaries, and a temperature- and depth-dependent rheology defined by the following non-dimensional formulation:

$$\eta(T, z) = \eta_0 e^{A(0.5-T)}, \tag{6}$$

where A is the activation coefficient and is equal to 9.21, leading to a 10^4 viscosity contrast due to temperature. η_0 is constant and equal to 1 in the upper mantle and 50 in the lower mantle (below 660 km), leading to a 50 times viscosity increase across the transition zone. Using such high temperature-dependent rheology typically leads to the formation of a rigid lid, which we eliminate by imposing a maximum allowable viscosity for the uppermost portion of the model, allowing strong slabs to form.

Following the procedure described in Refs. (*S5, S6*), we tracked deformation in tracers along several streamlines by computing the left-stretch tensor of each. The deformation gradient tensor $\mathbf{F}$ provides a complete description of finite deformation of a material,

$$\mathbf{F} = \begin{pmatrix} \frac{\partial s_x}{\partial x} + 1 & \frac{\partial s_x}{\partial y} \\ \frac{\partial s_y}{\partial x} & \frac{\partial s_y}{\partial y} + 1 \end{pmatrix} \tag{7}$$

where s_x and s_y are the x and y components of displacement in the initial reference frame. The evolution of $\mathbf{F}$ for a particular tracer is determined by integrating with the velocity gradient tensor, $\mathbf{L}$,

$$\frac{\partial}{\partial t}F_{ij} = L_{ik}F_{kj}, \tag{8}$$

with

$$\mathbf{L} = \begin{pmatrix} \frac{\partial v_x}{\partial x} & \frac{\partial v_x}{\partial y} \\ \frac{\partial v_y}{\partial x} & \frac{\partial v_y}{\partial y} \end{pmatrix} \tag{9}$$

where, v_x and v_y are the x and y components of velocity, respectively.

It is convenient to calculate the left Cauchy-Green deformation tensor, $\mathbf{B}$, which provides the deformation in the deformed coordinate system with rigid rotation and translation removed,

$$\mathbf{B} = \mathbf{F} \cdot \mathbf{F}^T. \tag{10}$$

From $\mathbf{B}$, it is simple to determine the left stretch tensor, $\mathbf{V}$, with

$$\mathbf{V}^2 = (\mathbf{V} \cdot \mathbf{R}) \cdot (\mathbf{R}^T \cdot \mathbf{V}) = \mathbf{F} \cdot \mathbf{F}^T = \mathbf{B} \tag{11}$$

$\mathbf{R}$ is an orthogonal tensor representing rigid rotation. Strain of a tracer is represented by the stretch which is the ratio of final length to original length. The principle directions and positive square roots of the eigenvalues of $\mathbf{V}^2$ are the directions and magnitudes of the maximum and minimum stretch, respectively.

4 Polycrystalline plasticity model and calculation of seismic velocities

Texture development along a streamline was simulated using the tangent approximation of the viscoplastic self-consistent model, as implemented in the Los Alamos VPSC code (*S7*). This polycrystal plasticity model relies on the concept of grain inclusions in a homogeneous

but anisotropic medium and is intermediate between the Taylor model that enforces strain compatibility and the Sachs model that is based on stress equilibrium. The model does not take grain interaction or intergranular heterogeneities into account but the VPSC has been reliable in simulating textures of many low symmetry materials (*S8*).

In the simulation, 2000 grains were deformed in 6433 steps along the streamline described in Fig. 3, S4 and S5, starting at the top of the D" layer, proceeding towards the core-mantle boundary, and later in an upwelling. Each deformation step was defined by a displacement gradient tensor obtained from the geodynamical model as described above. Activity of slip systems in all grains was evaluated in each step and orientations updated accordingly. From the orientation distribution of the 2000 grains, pole figures were calculated to illustrate crystal orientation patterns.

Bulk elastic constants of the polycrystal were calculated using the software package Beartex (*S4*), using the single crystal elastic moduli at 135 GPa and 4000 K of Stackhouse *et al.* (*S9*) and at 140 GPa and 4000 K from Wentzcovitch *et al.* (*S10*) (Table S3) and the ODF obtained from VPSC simulations. From the aggregate elastic tensor we then calculated and plotted seismic velocities in different directions using the petrophysics software package of D. Mainprice (*S11*) or Beartex (*S4*).

Accumulated strains along a streamline are very large (Fig. S5) and assuming that all this strain is accommodated by dislocation glide, polycrystal plasticity simulations predict very sharp textures, close to a single crystal. This is clearly not realistic. At high temperatures strain may be partially accommodated by climb and dynamic recrystallization that may significantly weaken texture development. Other considerations, including the presence of secondary phases, could also play a role. Therefore, we investigated the cases where 5%, 10%, and 50% of the strain provided by the geodynamic model is accommodated by dislocation glide in pPv and the rest by mechanisms that do not produce

preferred orientation.

Orientations and texture indices obtained along the streamline are presented in Fig. S6 and S7. Cases with 5 and 10% of the strain accommodated by dislocation glide in pPv produce similar texture patterns with a stronger texture intensity for the 10% case. With 50% of the strain accommodated by dislocation glide in pPv, the texture we obtain is close to a single crystal and is not realistic in a geophysical setting. The corresponding shear wave splittings are presented in Fig. S8, S9, and S10. In all cases, we find that most of the anisotropy strongly develops between the steps 1000 and 2000 near the turning point of downwelling. The strength of the anisotropy is strongly dependent on the amount of strain accommodated by dislocation glide in pPv with the 50% case displaying patterns very close to a single crystal. For both cases of elastic moduli, anisotropies obtained using a 5% or 10% hypothesis show a similar pattern but different amplitudes. Comparing the amount of shear wave splitting with those observed seismically, we selected the 10% case as our main reference model.

Figures

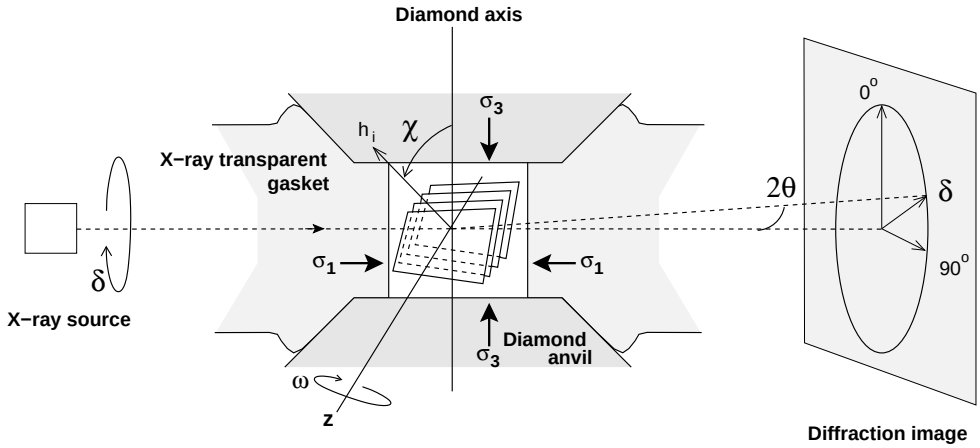

Fig. S1: Schematic of the experiment. The polycrystalline sample is confined under non-hydrostatic stress conditions between the two diamond anvils. σ_3 is the axial stress imposed by the diamonds and σ_1 the radial stress imposed by the gasket. A monochromatic x-ray beam is sent through the gasket and the data collected on an imaging plate orthogonal to the incoming beam. The position of the diffraction lines and intensity of diffraction are analyzed as a function of the azimuthal angle δ from which we calculate the angle χ between the normal to the diffracting plane h_i and the compression direction. In order to improve the statistics during data collection, we imposed oscillations of $\omega = \pm 2.5^\circ$ around the z-axis.

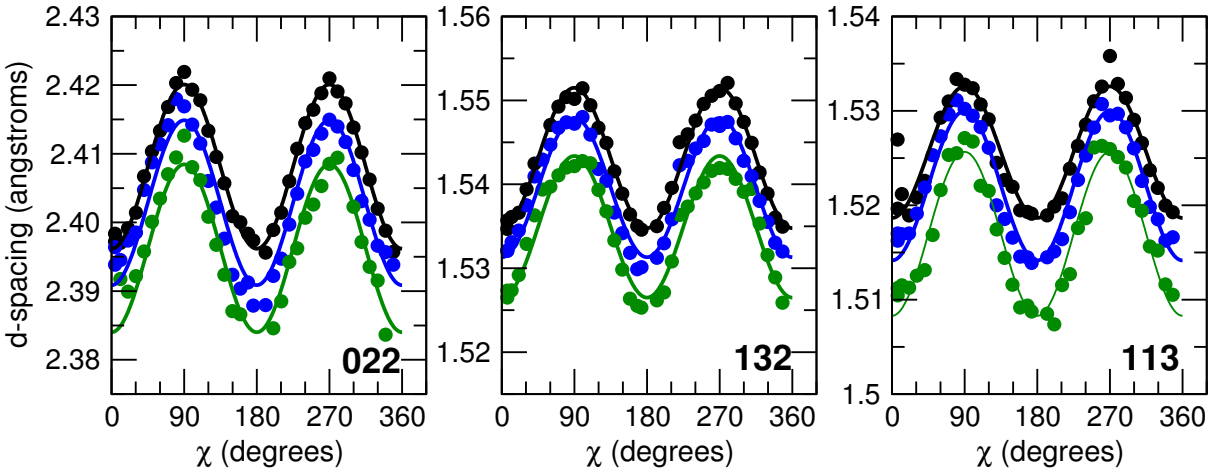

Fig. S2: Measured d-spacing (closed circles) and models used for lattice strain analysis (solid lines) as a function of the pole distance χ for the peaks 022, 132 and 113 of (Mg,Fe)SiO_3-pPv. Data in black, blue, and green correspond to pressures of 145, 150, and 157 GPa, respectively.

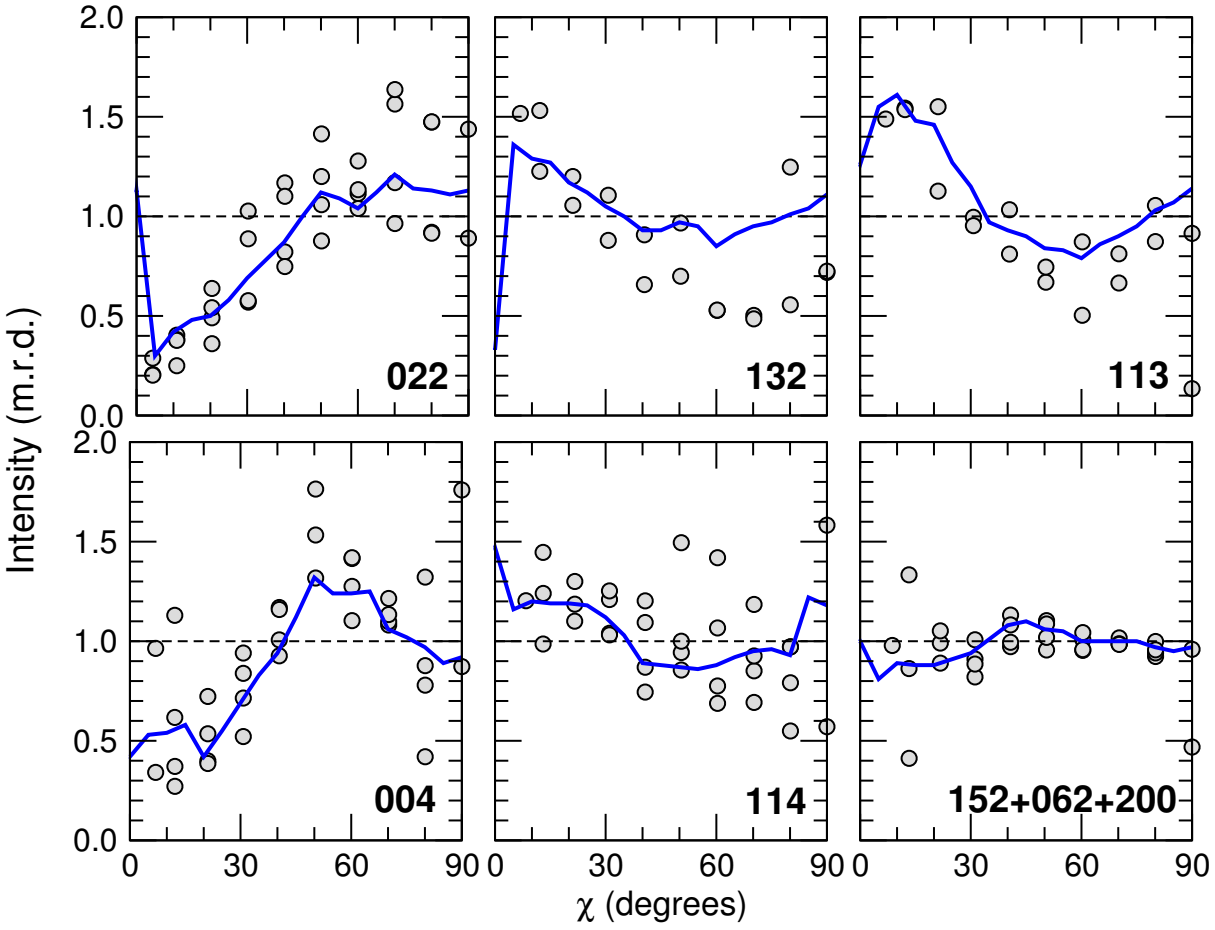

Fig. S3: Measured diffraction intensities (closed circles) and those recalculated from the orientation distribution function (solid blue lines) as a function of the pole distance from the compression direction χ for the 022, 132, 113, 004, 114, and 152+062+200 lines of (Mg,Fe)SiO_3-pPv at 145 GPa. Experimental intensities have been scaled to match those recalculated from the ODF, expressed in m.r.d., and pole distances have been converted to the $[0-90°]$ interval.

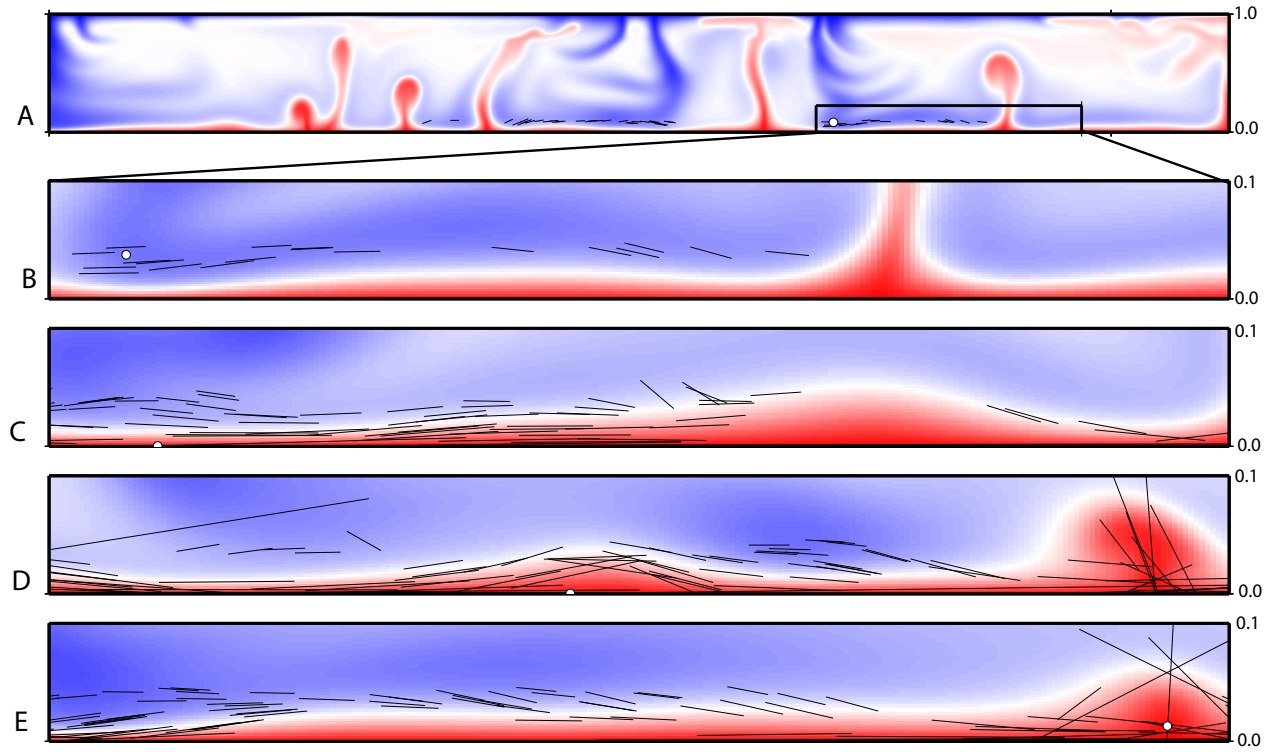

Fig. S4: Snapshots of 4 consecutive times of the convection calculation. Red represents hot material, and blue represents cold material. The tracer is represented by the white circle, and the black lines represent the maximum strain of various other tracers in the calculation. Z-positions are normalized so that $z = 0$ corresponds to the CMB, $z = 0.1$ to the top of D", and $z = 1$ at the Earth surface. Similarly, x-positions are normalized in units of mantle thickness so that $x = 1$ corresponds to 2890 km. A) the entire model domain at a time corresponding to the beginning of the tracking the deformation of the tracer. The inset black box represents a zoom-in view for other times. Zoom in views for B) 10 timesteps C) 2010 timesteps, D) 4010 timesteps, and E) 6010 timesteps.

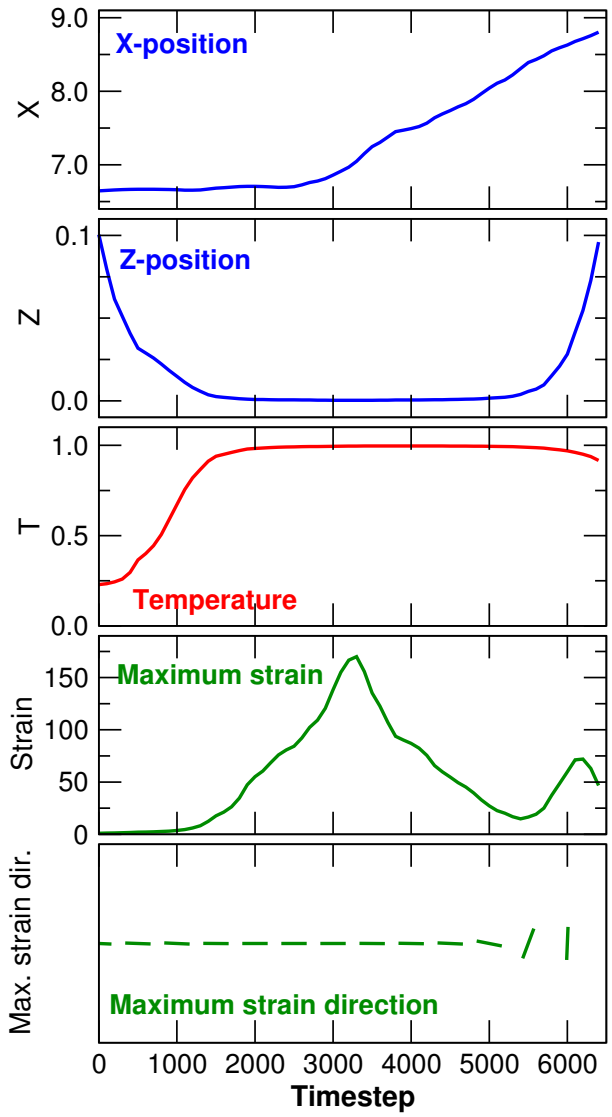

Fig. S5: Position, temperature, amplitude of the maximum strech of the Lagrangian particle, and orientation of the maximum strech of the Lagrangian particle recorded by the tracer as a function of timestep. Temperatures are normalized so that $T = 0$ at the Earth surface and $T = 1$ at the CMB, z-positions are normalized so that 0.1 corresponds to the top of D" and 0.0 to the CMB and, similarly, x-positions are normalized in units of mantle thickness so that $x = 1$ corresponds to 2890 km. In the last panel, the core-mantle boundary surface is horizontal.

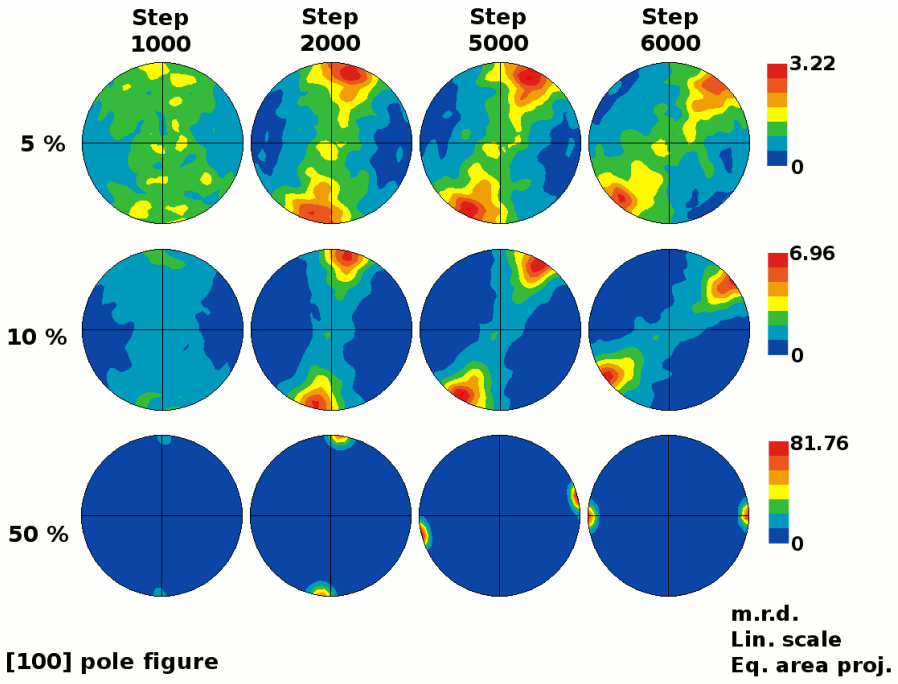

Fig. S6: Modelled three-dimensional [100] orientations in silicate post-perovskite at steps 1000, 2000, 5000, and 6000 for the simulations where 5%, 10%, and 50% of the strain provided by the geodynamic model is accommodated by dislocation glide in post-perovskite. Linear scale, equal area projection. Contours are expressed in multiples of a random distribution.

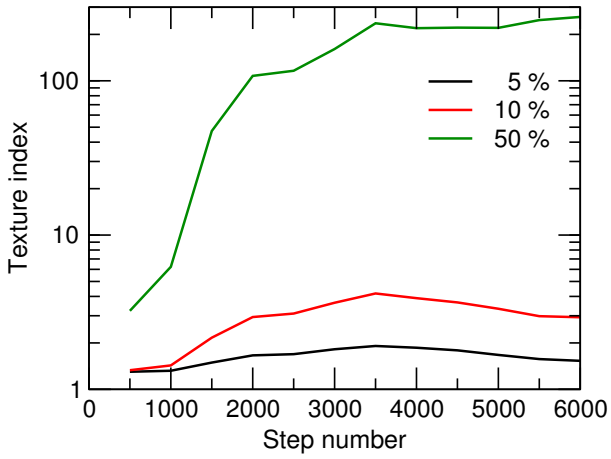

Fig. S7: Texture index vs. timestep for the simulations where 5%, 10%, and 50% of the strain provided by the geodynamic model is accommodated by dislocation glide in post-perovskite.

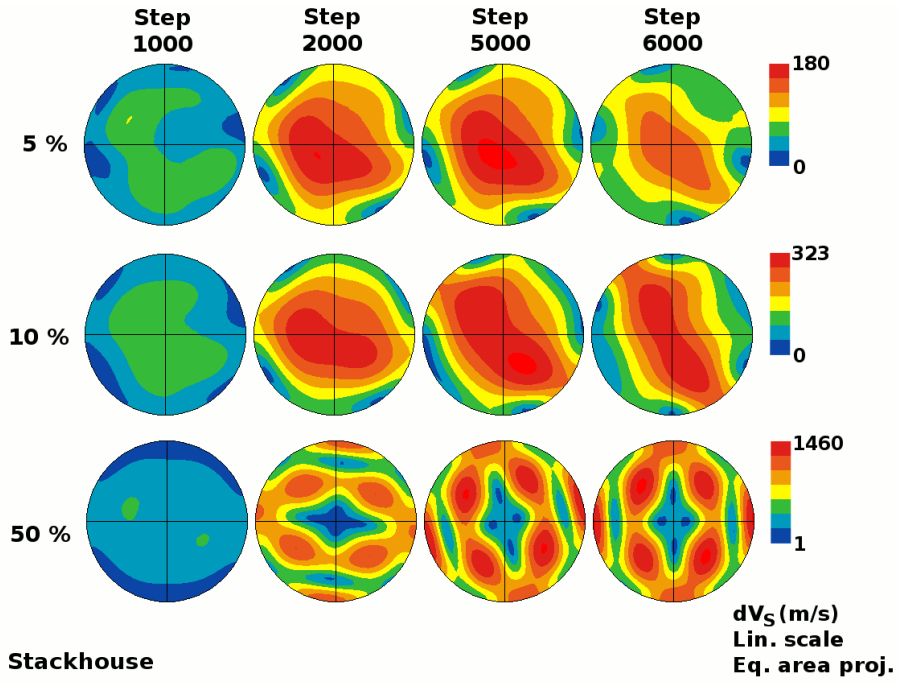

Fig. S8: Modelled shear wave splitting from silicate post-perovskite calculated using the elastic moduli of Stackhouse *et al.* (*S9*) at steps 1000, 2000, 5000, and 6000 for the simulations where 5%, 10%, and 50% of the strain provided by the geodynamic model is accommodated by dislocation glide in post-perovskite. Linear scale, equal area projection. Contours are expressed in m/s.

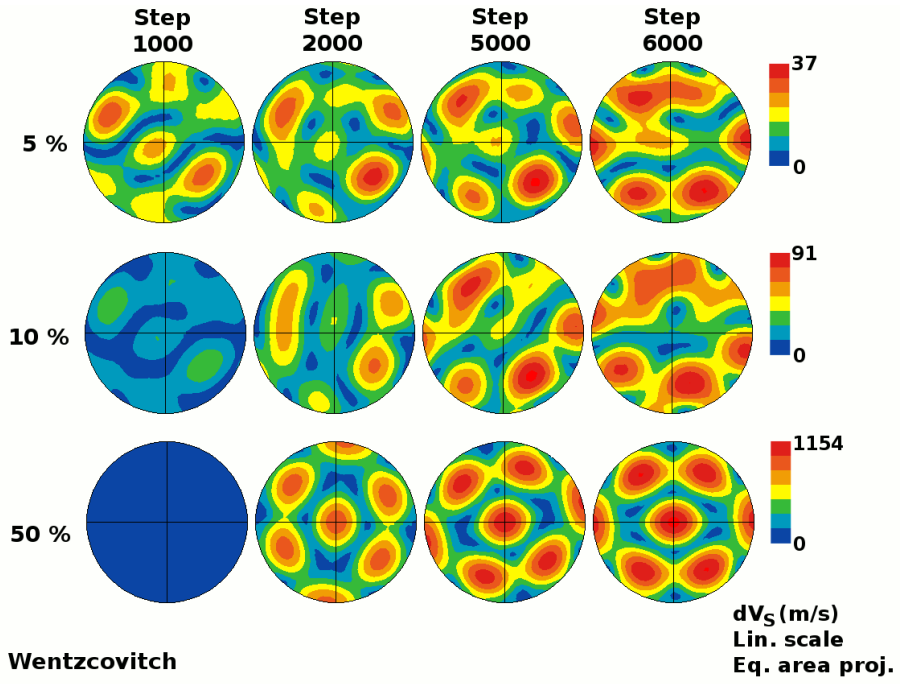

Fig. S9: Modelled shear wave splitting from silicate post-perovskite calculated using the elastic moduli of Wentzcovitch *et al.* (*S10*) at steps 1000, 2000, 5000, and 6000 for the simulations where 5%, 10%, and 50% of the strain provided by the geodynamic model is accommodated by dislocation glide in post-perovskite. Linear scale, equal area projection. Contours are expressed in m/s.

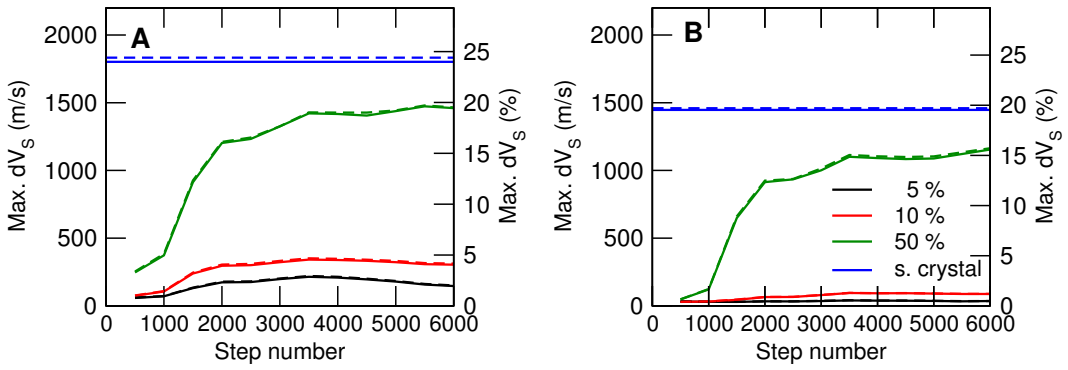

Fig. S10: Maximum shear wave splitting from silicate post-perovskite calculated using the elastic moduli of Stackhouse *et al.* (*S9*) (A) and Wentzcovitch *et al.* (*S10*) (B) expressed in m/s (solid lines) or in percents (dashed lines) vs. timestep for the simulations where 5% (black line), 10% (red line), and 50% (green line) of the strain provided by the geodynamic model is accommodated by dislocation glide in post-perovskite. For reference, the largest shear wave splitting value obtained for a single crystal is shown in blue.

Tables

Table S1: Pressure, average lattice strain $<Q>$, differential stress t, unit cell parameters, a, b, and c, and texture index F_2 measured in (Mg,Fe)SiO_3-pPv. Numbers in parenthesis are the uncertainties on the last digit.

Name	P (GPa)	$<Q>$*1000	t (GPa)	a ($\AA$)	b ($\AA$)	c ($\AA$)	F_2
P01	145	3.17(4)	7.2(1)	2.439(4)	7.956(7)	6.063(4)	1.357
P02	150	3.36(6)	7.7(1)	2.436(3)	7.935(5)	6.050(3)	1.216
P03	157	3.60(8)	8.5(2)	2.425(5)	7.911(9)	6.034(6)	1.221

Table S2: Slip systems, critical resolved shear stress (CRSS) ratios, and slip systems activities at step 2000 in the simulations where 10% of the strain provided by the geodynamic model is accommodated by dislocation glide in post-perovskite.

System	(100) <001>	(100) <010>	(110) <110>	(110) <001>	(001) <100> (001) < 110 > (001) <010>
CRSS	2	1	1	4	10
Activity	18%	12%	56%	8%	6%

Table S3: Elastic moduli used for calculating seismic anisotropies. Pressures and elastic moduli are expressed in GPa and temperatures in K.

	P	T	C_{11}	C_{22}	C_{33}	C_{12}	C_{23}	C_{23}	C_{44}	C_{55}	C_{66}
Stackhouse *et al.* (*S9*)	135	4000	1107	847	1131	429	318	441	251	221	361
Wentzcovitch *et al.* (*S10*)	140	4000	1119	900	1131	498	486	536	343	231	326

References and Notes

S1. S. R. Shieh, *et al.*, *Proc. Nat. Acad. Sc.* **103**, 3039 (2006).

S2. A. K. Singh, C. Balasingh, H. K. Mao, R. J. Hemley, J. Shu, *J. Appl. Phys.* **83**, 7567 (1998).

S3. T. Tsuchiya, J. Tsuchiya, K. Umemoto, R. M. Wentzcovitch, *Geophys. Res. Lett.* **31**, L14603 (2004).

S4. H. R. Wenk, S. Matthies, J. Donovan, D. Chateigner, *J. Appl. Cryst.* **31**, 262 (1998).

S5. A. K. McNamara, P. E. van Keken, S.-I. Karato, *J. Geophys. Res.* **108**, 2230 (2003).

S6. H.-R. Wenk, S. Speziale, A. K. McNamara, E. J. Garnero, *Earth Planet. Sci. Lett.* **245**, 302 (2006).

S7. R. A. Lebensohn, C. N. Tomé, *Acta Metall. Mater.* **41**, 2611 (1993).

S8. H. R. Wenk, *Model. Simul. Mater. Sci. Engin.* **7**, 699 (1999).

S9. S. Stackhouse, J. P. Brodholt, J. Wookey, J.-M. Kendall, G. D. Price, *Earth Planet. Sci. Lett.* **230**, 1 (2005).

S10. R. Wentzcovitch, T. Tsuchiya, J. Tsuchiya, *Proc. Nat. Acad. Sc.* **103**, 543 (2006).

S11. D. Mainprice, *Computers & Geosciences* **16**, 385 (1990).